Journal of Materials Chemistry A

ROYAL SOCIETY OF CHEMISTRY

PAPER

Cite this: *J. Mater. Chem. A*, 2020, **8**, 18816

Sacrificial agent-free photocatalytic H_2O_2 evolution *via* two-electron oxygen reduction using a ternary α-Fe_2O_3/CQD@g-C_3N_4 photocatalyst with broad-spectrum response†

Xi Chen,[ab] Wenwen Zhang,[b] Lixiang Zhang,[bc] Luping Feng,[ab] Chunxian Zhang,[b] Jie Jiang,[d] Tingjiang Yan[b] and Hua Wang *[abd]

Received 9th June 2020
Accepted 6th August 2020

DOI: 10.1039/d0ta05753c

rsc.li/materials-a

Ultrathin g-C_3N_4 nanosheets have been fabricated *via* a two-step calcination regulated by melamine precursors at a high heating rate (30 °C min^{-1}). The resulting g-C_3N_4 nanosheets were further employed as carriers for the growth of carbon quantum dots (CQDs) and (110) exposed α-Fe_2O_3 through the PVP-enabled adsorption effects by a solvothermal process. It was discovered that the so fabricated ternary photocatalyst α-Fe_2O_3/CQD@g-C_3N_4 presented a broad-spectrum absorption range (up to 800 nm) and particularly enhanced active sites of photogenerated electrons for highly efficient photocatalytic oxygen reduction toward H_2O_2 evolution in pure water. A H_2O_2 production rate of 1.16 μM min^{-1} could be expected for the developed photocatalyst under visible light irradiation, which is about 19 times faster than that of pure ultrathin g-C_3N_4. Herein, the loaded Fe_2O_3 could transform the H_2O_2 evolution from two-step single-electron reduction into one-step two-electron one, as verified by the various active species experiments and rotating ring-disk electrode tests. This work presents a new perspective in designing ultrathin g-C_3N_4 through a simple method of precursor-regulated calcination, which features more outstanding advantages than the conventional exfoliation of bulk g-C_3N_4 towards ultrathin g-C_3N_4. More importantly, it provides an optimized photocatalytic reaction route of two-electron oxygen reduction for efficient H_2O_2 production in pure water under visible light irradiation, without the need for noble metals or organic sacrificial agents.

Introduction

As an eco-friendly oxidant, hydrogen peroxide (H_2O_2) has been widely applied in the fields of medical disinfection, cosmetics industry, and wastewater treatment.[1–3] Recently, photocatalytic H_2O_2 production techniques, especially those driven by renewable and sufficient sunlight, have attracted much attention to stand a chance of substituting the traditional ones with anthraquinone processes.[4–6] However, high H_2O_2 yields have generally been acquired by using noble metals or organic sacrificial agents to facilitate the efficient separation of photogenic electron–hole pairs, which may go against the manufacturing cost or product purification for large-scale industrialization.[7–9] Hence, fabricating a cost-effective and green photocatalyst for highly efficient H_2O_2 evolution in pure water has been an attractive target to pursue.

In recent years, graphitic carbon nitride (g-C_3N_4) has been increasingly employed as a green metal-free material in the photocatalytic field.[10–21] However, g-C_3N_4 in the bulk format may suffer from some inherent defects such as rapid charge-carrier recombination, low electronic conductivity, and small specific surface area, which may limit its large-scale applications.[22–24] Alternatively, some endeavors have recently been devoted to preparing ultrathin or even single-layer g-C_3N_4.[25–27] Inspired by the layering of graphene from bulk graphite, exfoliation methods have commonly been employed to produce ultrathin g-C_3N_4 from bulk g-C_3N_4, such as the hyperthermia solvothermal process, hydrochloric acid protonation and alcohol sonication.[28–31] Nevertheless, these top-down methods require the fabrication of high-quality bulk materials, making them more fussy and time-consuming. Therefore, a simple and efficient synthesis of ultrathin g-C_3N_4 nanosheets is a challenging issue.

[a]*School of Chemistry and Chemical Engineering, Harbin Institute of Technology, Harbin, Heilongjiang 150090, P. R. China*

[b]*Institute of Medicine and Materials Applied Technologies, College of Chemistry and Chemical Engineering, Qufu Normal University, Qufu, Shandong 273165, P. R. China. E-mail: huawang@qfnu.edu.cn; Web: http://wang.qfnu.edu.cn; Tel: +86 537 4456306*

[c]*School of Environment, Harbin Institute of Technology, Harbin, Heilongjiang 150090, P. R. China*

[d]*School of Marine Science and Technology, Harbin Institute of Technology at Weihai, Weihai, Shandong 264209, P. R. China*

† Electronic supplementary information (ESI) available. See DOI: 10.1039/d0ta05753c

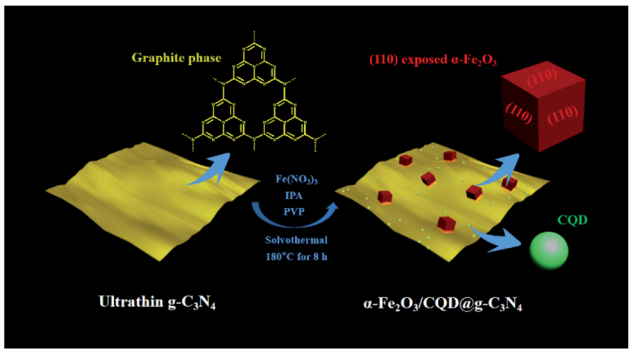

Scheme 1 Schematic illustration of the synthesis of the α-Fe_2O_3/CQD@g-C_3N_4 ternary photocatalyst *via* a solvothermal process, where CQDs and (110) exposed α-Fe_2O_3 were decorated onto g-C_3N_4 nanosheets in the presence of PVP using IPA and $Fe(NO_3)_3$ as the precursors.

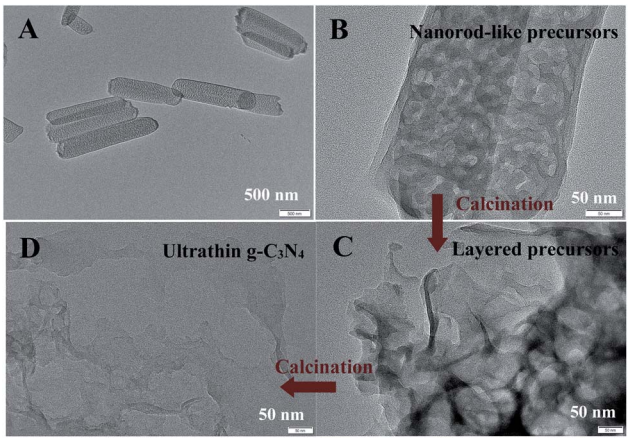

Fig. 1 TEM images of the products obtained in the step-by-step calcination procedure towards ultrathin g-C_3N_4. (A) nanorod-like precursors; (B) amplified image; (C) layered precursors; (D) ultrathin g-C_3N_4.

Moreover, recent years have witnessed the rapid development of another type of eco-friendly material, namely carbon quantum dots (CQDs) as the active sites of photocatalysis, because they possess the properties of fast charge transfer, excellent photo-generated electron capture, and efficient up-conversion.[32,33] Besides, α-Fe_2O_3 especially the one with exposed (110) has been demonstrated to have an excellent O_2 adsorption capacity.[34]

In the present work, ultrathin g-C_3N_4 nanosheets were fabricated *via* a two-step calcination of melamine precursors without the need for complicated pre- and post-processing steps. The obtained g-C_3N_4 nanosheets were further used as carriers for the growth of CQDs and α-Fe_2O_3 *via* a solvothermal process in the presence of PVP, yielding the ternary photocatalyst α-Fe_2O_3/CQD@g-C_3N_4, and the main procedure is schematically illustrated in Scheme 1. Here, CQDs were employed to remedy the drawback of ultrathin g-C_3N_4 regarding the broad band gap. Also, α-Fe_2O_3 with exposed (110) might serve as the photocatalytic active center for H_2O_2 evolution. The so established carrier transfer pathway of α-Fe_2O_3/CQD@g-C_3N_4 was further confirmed by the removal experiments of reactive species and DMPO electron spin resonance, in addition to the explanation obtained by the energy band structure analysis. Of note, herein, the construction of ultrathin g-C_3N_4 nanosheets was achieved through a precursor-regulated direct calcination route, and they served as the carriers for the growth of CQDs and α-Fe_2O_3 toward a superior ternary photocatalyst for efficient H_2O_2 production under visible light, without the need for noble metals or organic scavengers.

Results and discussion

Preparation and characterization of ultrathin g-C_3N_4

Ultrathin g-C_3N_4 nanosheets were prepared directly by calcining melamine precursors through a two-step rapid heating process (30 °C min^{-1}), which may be completely different from the conventional top-down exfoliation way. The products yielded in the step-by-step calcination procedure were monitored by TEM imaging and the data are shown in Fig. 1. As shown in Fig. 1A, nanorod-like precursors derived from glycol-intercalated cyanuric acid were first obtained through the hydrolysis of melamine at room temperature showing a mesoporous structure with long interlamellar distance, as disclosed clearly in the amplified image (Fig. 1B). During the calcination at 450 °C with a rapid heating, layered precursors were achieved due to the airflow produced from glycol-intercalated cyanuric acid derivatized with abundant –NH_2 and –OH groups, resulting in a decreased interlamellar distance (Fig. 1C). Furthermore, thermal-polymerization of the layered precursors could occur during the continuous calcination at a higher temperature of 550 °C, yielding ultrathin g-C_3N_4 nanosheets (Fig. 1D).

Synthesis and characterization of α-Fe_2O_3/CQD@g-C_3N_4

Herein, the α-Fe_2O_3/CQD@g-C_3N_4 composites were prepared alternatively through decorating g-C_3N_4 nanosheets with (110) exposed α-Fe_2O_3 and CQDs *via* a solvothermal process in the presence of PVP, as illustrated in Scheme 1. Fig. 2 manifests the TEM images of the α-Fe_2O_3/CQD@g-C_3N_4 nanosheets so

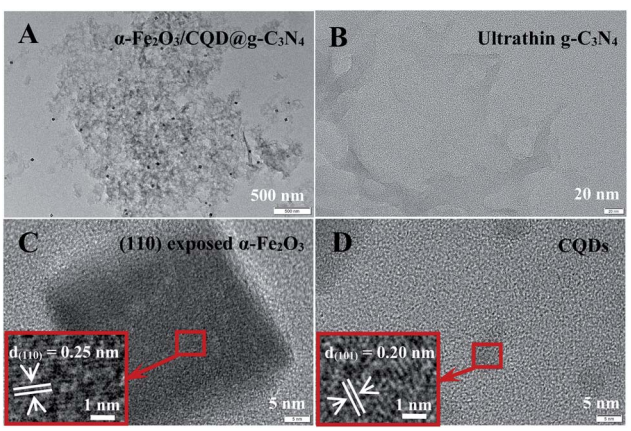

Fig. 2 (A) TEM image of α-Fe_2O_3/CQD@g-C_3N_4, and the magnification-amplified TEM images of (B) ultrathin g-C_3N_4, (C) α-Fe_2O_3 and (D) CQDs.

produced. As can be seen from Fig. 2A, the ultrathin g-C_3N_4 consists of thin layers with low density. Herein, the curled edges of the nanosheets may demonstrate the ultrathin structure owing to the minimization of surface energy,[35] as also revealed by the transparent character of the image (Fig. 2B and S1†). Additionally, Fig. S2† displays the close connection among α-Fe_2O_3, CQDs, and g-C_3N_4 nanosheets, which can be witnessed more clearly in the magnification-amplified parts. PVP as a nonionic polymer compound was employed to integrate the g-C_3N_4 with α-Fe_2O_3 and CQDs so as to obtain the synergistic effect achieving the boosted carrier transfer. Moreover, as shown in Fig. 2C, the quasicubic α-Fe_2O_3 could be observed with a spacing of 0.25 nm on the surface of g-C_3N_4 nanosheets, thus validating the exposure of the (110) facet.[36,37] Compared to the other crystal facets of Fe_2O_3, of note, the (110) facet with a relatively high density of iron atoms (10.1 atoms per nm^2) might present a stronger interaction with oxygen so as to enhance the surface oxygen content of the photocatalyst, which might improve the photocatalytic H_2O_2 production *via* the oxygen reduction reaction.[34,38] Furthermore, Fig. 2D confirms the existence of CQDs with a spacing of 0.20 nm, showing a graphite-like structure with a size of 6 nm diameter.[33] These above morphological characteristics indicate that the α-Fe_2O_3/CQD@g-C_3N_4 composites were successfully synthesized.

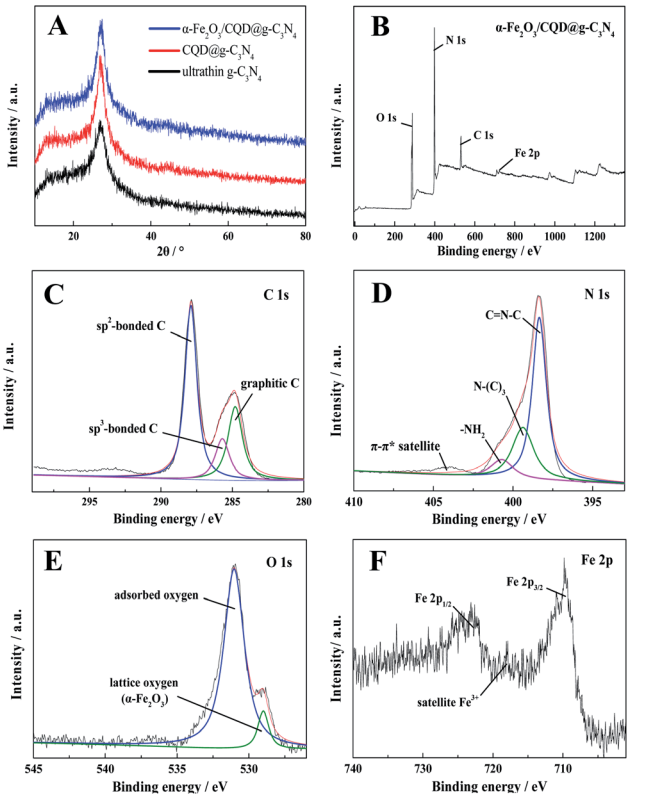

Fig. 3 (A) XRD patterns of different samples; (B) XPS spectra of α-Fe_2O_3/CQD@g-C_3N_4, with (C) C1s, (D) N1s, (E) O1s, and (F) Fe2p.

Phase structure and surface elemental composition

X-ray diffraction (XRD) was conducted to determine the phase structure of the α-Fe_2O_3/CQD@g-C_3N_4 composites by comparing with pure g-C_3N_4 and CQD@g-C_3N_4, and the results are shown in Fig. 3A. The diffraction peaks at 2θ values of 13.2° and 27.3° correspond to the (100) and (002) facets of g-C_3N_4, respectively, which can separately represent the in-plane packing motif and interlayer stacking, indicating that the phase structure of the carriers can be well indexed to graphitic carbon nitride (JCPDS no. 87-1526).[39] Moreover, the significant broadening of the main diffraction peak from 15° to 35° may embody the small size of the samples, suggesting the successful formation of ultrathin g-C_3N_4. It is a pity that no diffraction peaks of CQDs or α-Fe_2O_3 can be observed, presumably because they might present a uniform distribution in composites with the peaks largely covered by the broadened peak of g-C_3N_4. Yet, the α-Fe_2O_3/CQD@g-C_3N_4 composites could exhibit a g-C_3N_4 pattern similar to that of pure g-C_3N_4 and CQD@g-C_3N_4, implying that the structures of g-C_3N_4 carriers could be well sustained after the integration with CQDs and α-Fe_2O_3.

The chemical states of the elements in α-Fe_2O_3/CQD@g-C_3N_4 composites were explored by X-ray photoelectron spectroscopy (XPS). As shown in Fig. 3B, C, N, O, and Fe elements are spread on the surface of the composites, and the relative contents are shown in Table S1.† Moreover, the peaks with binding energies of 284.8, 285.7, and 287.9 eV are indexed to graphitic carbon, sp^3-coordinated carbon bonds, and sp^2-bonded carbon in the developed composite, respectively (Fig. 3C).[40] Also, the signals of C≡N and C–C could be ascribed to the bonding manner of g-C_3N_4. Furthermore, one can find from Fig. 3D that the peaks situated at 398.4, 399.4, 400.7 and 404.1 eV refer to C=N–C, N–$(C)_3$, $-NH_2$ and π–π* satellite, respectively, revealing the characteristic signal of nitrogen from g-C_3N_4.[41] As can be observed from Fig. 3E, the binding energy of 528.9 eV should be assigned to the lattice oxygen of α-Fe_2O_3 in the composites. Fig. 3F manifests that the peaks at binding energies of 710.0 and 722.4 eV are the split signals of $Fe2p_{3/2}$ and $Fe2p_{1/2}$, respectively, where the satellite at 717.9 eV should be related to the trivalent Fe element.[42] Besides, the bulk loading amount of Fe_2O_3 was calculated to be about 12.3% according to the XPS measurements for obtaining the elemental contents in the composites.

Light absorption properties and charge carrier behavior

It is commonly recognized that the light harvesting capacity is one of the vital factors for the performance of photocatalysts. Herein, UV-vis diffuse reflectance spectra were recorded for the different products (Fig. 4A). One can see that ultrathin g-C_3N_4 can present an absorption edge at about 441 nm, which may exhibit a noticeable red-shift once loaded with α-Fe_2O_3. Fig. 4B discloses the up-conversion fluorescence spectra of CQDs under visible light and near infrared light (*i.e.*, 800 nm) irradiation. As expected, CQDs can feature the highest fluorescence emission intensity at about 445 nm, which is very close to the absorption edge of carbon nitride (441 nm). The data indicate that the minimum excitation wavelength of the α-Fe_2O_3/CQD@g-C_3N_4 composite might be expanded to the near infrared range (*i.e.*, 800 nm) on account of the up-conversion of the CQDs loaded.

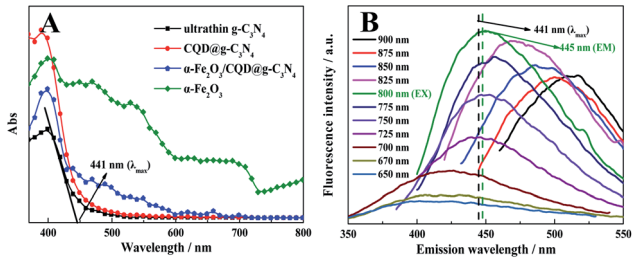

Fig. 4 (A) UV-vis DRS spectra of g-C_3N_4, CQD@g-C_3N_4, α-Fe_2O_3/CQD@g-C_3N_4, and α-Fe_2O_3. (B) Up-conversion fluorescence spectra of CQDs.

The band structure of α-Fe_2O_3/CQD@g-C_3N_4 was investigated aiming to comprehend the charge carrier behavior (Fig. 5). Herein, the band gaps of g-C_3N_4 and α-Fe_2O_3 were estimated according to the following formula: $\alpha h\nu = A(h\nu - E_g)^2$,[43,44] and the results of 2.81 and 2.17 eV are shown in Fig. 5A. Moreover, based on the Nernst equation: $E_{RHE} = E_{Ag/AgCl} + 0.05916\ pH + E0Ag/AgCl$,[45,46] the Mott–Schottky test was carried out to explore the conduction band potential of g-C_3N_4 (Fig. 5B). It is found that the positive slope of plots indicates that g-C_3N_4 is an n-type semiconductor, whose conduction band nearly verges on the flat band. Also, the potential of the conduction band (E_{CB}) of g-C_3N_4 is calculated to be −1.13 eV (*vs.* NHE). Similarly, the E_{CB} of α-Fe_2O_3 is calculated to be 0.26 eV (*vs.* NHE). The band potentials of α-Fe_2O_3 and g-C_3N_4 are ultimately listed in Table S2.†

Fig. 5C describes the data of electrochemical impedance spectroscopy (EIS) for confirming the charge carrier behavior of the α-Fe_2O_3/CQD@g-C_3N_4 composite by the route described previously.[47] One can see that the semicircle radius of CQD@g-C_3N_4 is smaller than that of pure g-C_3N_4, indicating that CQDs have efficiently improved the charge transfer capacity of ultrathin g-C_3N_4. Also, an analogous result was obtained for α-Fe_2O_3/CQD@g-C_3N_4, which should provide evidence of heterojunctions with accelerated carrier transfer due to its smallest semicircle radius. Moreover, the carrier separation efficiencies were investigated and the results are shown in Fig. 5D. Compared with CQD@g-C_3N_4, the Fe_2O_3@g-C_3N_4 presents a more efficient separation of photogenerated electron–hole pairs, suggesting that the photoelectrons in ternary composites can be readily transferred from g-C_3N_4 to Fe_2O_3.

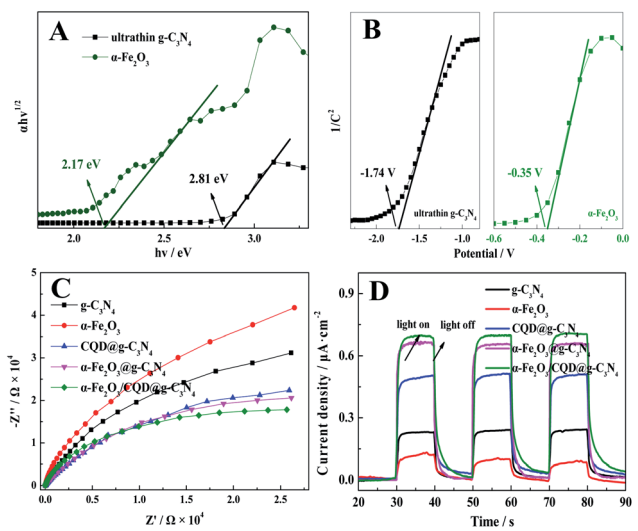

Fig. 5 (A) Plots of $(\alpha h\nu)^{1/2}$ *versus* energy ($h\nu$) of g-C_3N_4 and α-Fe_2O_3; (B) Mott–Schottky plots of g-C_3N_4 and α-Fe_2O_3 obtained at 1000 Hz; (C) electrochemical impedance spectra and (D) transient photocurrent responses of different samples.

Photocatalytic performances

To evaluate the photocatalytic activities of different samples, H_2O_2 production experiments were carried out comparably under visible light irradiation. As can be seen from Fig. 6A, the H_2O_2 production rates were 0.03, 0.005, 0.01, 0.15, 0.73 and 0.91 μM min^{-1} for g-C_3N_4, α-Fe_2O_3, CQDs, CQD@g-C_3N_4, α-Fe_2O_3@g-C_3N_4, and α-Fe_2O_3/CQD@g-C_3N_4 in O_2-equilibrated water as well as being 0.06, 0.02, 0.03, 0.31, 0.96 and 1.16 μM min^{-1} for those in O_2-saturated water (Fig. 6B and C), respectively. One can note that a higher concentration of dissolved oxygen in water could effectively provide an improved production rate of H_2O_2. More importantly, the photocatalytic performances of α-Fe_2O_3/CQD@g-C_3N_4 for H_2O_2 production were compared to those of some photocatalysts reported elsewhere, and the data are summarized in Table S3.† It is noted

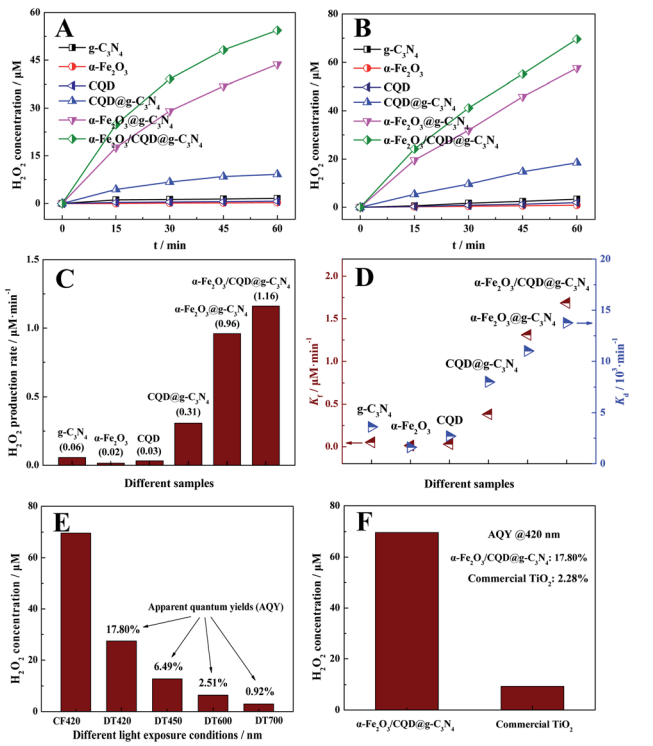

Fig. 6 (A) Photocatalytic H_2O_2 production amounts of different samples in (A) O_2-equilibrated water and (B) O_2-saturated water; (C) H_2O_2 production rates in O_2-saturated water; (D) K_f and K_d values for H_2O_2 production of various samples; (E) H_2O_2 production and apparent quantum yields (AQY) of α-Fe_2O_3/CQD@g-C_3N_4 under different monochromatic light; (F) comparison of H_2O_2 production and AQYs of the samples under visible light @ 420 nm.

that the developed ternary composite can present a H_2O_2 yield rate of 138.6 μmol g^{-1} h^{-1} at 5.0 mg photocatalyst, which is much higher than that of most current photocatalysts like g-C_3N_4 composites, and comparable to that of the ones with noble metal cocatalysts. In addition, the process of photocatalytic H_2O_2 production usually involves the formation and decomposition of H_2O_2. In consequence, the zero-order kinetics (H_2O_2 formation) and first-order kinetics (H_2O_2 decomposition) were established to assess the behavior of H_2O_2 production using the kinetics model shown as follows:[48]

$$[H_2O_2] = \frac{K_f}{K_d}(1 - \exp(-K_d t))$$

where K_f and K_d represent the H_2O_2 formation and decomposition rate (μM min^{-1}), which are calculated by fitting the data in Fig. 6B based on the above kinetics model, and the results are displayed in Fig. 6D. The K_f values of g-C_3N_4 were prominently enhanced by the addition of α-Fe_2O_3, but the K_d value was not. The results reveal that the combination of g-C_3N_4 with α-Fe_2O_3 could dramatically accelerate the H_2O_2 formation and inhibit H_2O_2 decomposition due to the construction of an efficient heterojunction.

Fig. 6E illustrates the H_2O_2 production capacities and apparent quantum yields (AQY) of α-Fe_2O_3/CQD@g-C_3N_4 under different monochromatic light exposure. It can be seen that the composite features a favorable yield of H_2O_2 with an AQY of 17.80% at 420 nm. What's more, this composite also embodies considerable photocatalytic activities, and its absorption edge is greater than that of pure g-C_3N_4 (441 nm), which is ascribed to the excellent up-conversion of CQDs. In particular, α-Fe_2O_3/CQD@g-C_3N_4 shows an AQY of 6.49% at 450 nm, which is referred to the maximum up-conversion intensity of CQDs under light irradiation (Fig. 4B), and even sustains a value of 0.92% at 700 nm. These results attest that the up-conversion of CQDs observably enhances the light utilization efficiency of the composite, thus raising the H_2O_2 production. Furthermore, the comparable investigations in Fig. 6F indicate that a-Fe_2O_3/CQD@g-C_3N_4 could exhibit >7.5 times higher amount of H_2O_2 evolution than commercially available TiO_2 under visible light irradiation, showing an excellent photocatalytic activity with an AQY of 17.80% at 420 nm, which is even far more than that of TiO_2 (2.28% at 420 nm).

The stability tests of photocatalytic H_2O_2 evolution were carried out by using α-Fe_2O_3/CQD@g-C_3N_4 under the same photocatalytic conditions (Fig. S3A†). To our surprise, only 4% deactivation was observed in the fifth run, indicating that the developed ternary composite can well sustain an excellent photostability for long-term application. Not only that, it is found that the XRD patterns (Fig. S3B†) of the composite exhibit no obvious variation after several photocatalytic reactions, indicating that this ternary photocatalyst can still retain the satisfactory crystal structure.

Active species experiments

Superoxide radical ($\cdot O_2^-$) removal experiments were first conducted to confirm the active species during the photocatalytic reactions.[49,50] As shown in Fig. 7A, the photocatalytic activity of CQD@g-C_3N_4 could be completely restrained by *p*-benzoquinone (BQ), showing that the generation of H_2O_2 could just be dependent on the abundant $\cdot O_2^-$. In contrast, the α-Fe_2O_3/CQD@g-C_3N_4 could well sustain a highly efficient H_2O_2 production in the presence of BQ, indicating that the H_2O_2 was not primarily generated by $\cdot O_2^-$ in this system. Not only that, DMPO spin-trapping ESR spectra are given to further substantiate the results of the active species experiments.[51] Fig. 7B shows that the signals of DMPO–$\cdot O_2^-$ produced by the CQD@g-C_3N_4 and α-Fe_2O_3/CQD@g-C_3N_4 were detected after 10 min irradiation of visible light for H_2O_2 production. Four strong characteristic peaks were observed for CQD@g-C_3N_4, whereas quite weak signals were found for the ternary composite, demonstrating that $\cdot O_2^-$ was not the main active species of α-Fe_2O_3/CQD@g-C_3N_4 during photocatalysis.

To further verify the active species of photocatalytic H_2O_2 production by CQD@g-C_3N_4 and α-Fe_2O_3/CQD@g-C_3N_4, the superoxide radical ($\cdot O_2^-$) evolution could be investigated using NBT, which was employed as an $\cdot O_2^-$ scavenger and subsequently degraded by $\cdot O_2^-$ during the photocatalysis.[52] From Fig. 7C it is discovered that the NBT was more effectively degraded by CQD@g-C_3N_4 than by α-Fe_2O_3/CQD@g-C_3N_4. Only a very few $\cdot O_2^-$ radicals were evolved by the developed ternary composite, although it could present a higher H_2O_2 production. The results reveal that the α-Fe_2O_3 has converted the H_2O_2 production pathway of α-Fe_2O_3/CQD@g-C_3N_4 from the two-step single-electron reduction into the direct one-step two-electron reduction.

Considering that H_2O_2 may be acquired through the reaction of hydroxyl radicals (·OH), ·OH removal experiments were

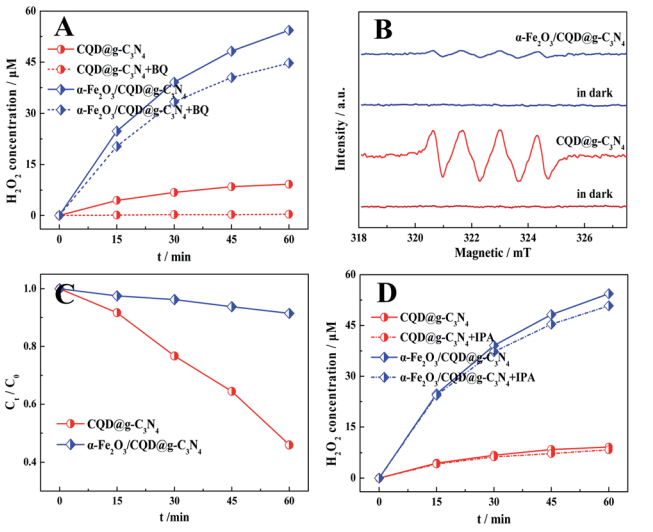

Fig. 7 (A) Reactive species trapping results of CQD@g-C_3N_4 and α-Fe_2O_3/CQD@g-C_3N_4 in the absence and presence of BQ (1.0 mM) in O_2-equilibrated water; (B) DMPO–$\cdot O_2^-$ spin-trapping ESR spectra of CQD@g-C_3N_4 and α-Fe_2O_3/CQD@g-C_3N_4 for H_2O_2 production before and after 10 min illumination; (C) photocatalytic NBT decomposition (2.5 mM) of CQD@g-C_3N_4 and α-Fe_2O_3/CQD@g-C_3N_4 in the H_2O_2 production process; (D) reactive species trapping results of CQD@g-C_3N_4 and α-Fe_2O_3/CQD@g-C_3N_4 in the absence and presence of IPA (1.0 mM) in O_2-equilibrated water.

carried out (Fig. 7D), which may help us to understand the contribution of ·OH to photocatalytic H_2O_2 generation.[53,54] As expected, the photocatalytic activities of these photocatalysts mentioned above might not be obviously affected by the ·OH quencher isopropanol (IPA). Therefore, the water should be directly oxidized to H_2O_2 mainly by the photogenerated holes, without the formation of ·OH.

Photocatalytic mechanism

To confirm the photocatalytic pathway towards H_2O_2, the rotating ring-disk electrode (RRDE) technique was carried out during the oxygen reduction reaction (ORR), in which the main product was considered as H_2O_2 in neutral solution similar to the photocatalytic conditions. The measured disk and ring currents of CQD@g-C_3N_4 and a-Fe_2O_3/CQD@g-C_3N_4 are displayed in Fig. 8A, and the apparent electron transfer number (n) could be calculated from Fig. 8A using the following equation:[55]

$$n = \frac{4J_D}{J_D + \frac{J_R}{N}}$$

where J_D and J_R are the disk and ring current densities, respectively. The officially provided collection efficiency (N) is determined to be 37%. As shown in Fig. 8B, the α-Fe_2O_3/CQD@g-C_3N_4 could achieve a calculated n value close to 2, thereby it goes through the 2-electron pathway with H_2O_2 as the primary reduction product. However, the n value of CQD@g-C_3N_4 was calculated to be 3, which greatly exceeded 2, indicating the difficult production of H_2O_2 *via* the 2-electron pathway. These results were in well agreement with those of active species experiments, further demonstrating that the developed ternary composite could feature a two-electron transfer mechanism for H_2O_2 production in neutral solution.

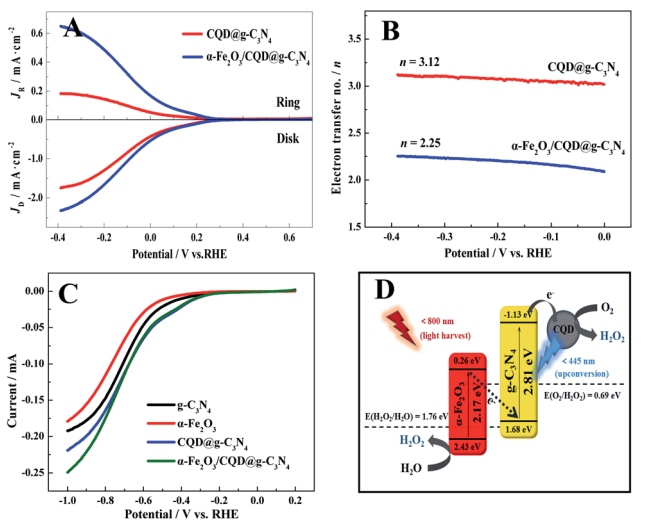

Fig. 8 (A) RRDE curves of α-Fe_2O_3/CQD@g-C_3N_4 measured at 1600 rpm in 0.10 M PBS; (B) electron transfer numbers at different potentials calculated from RRDE data; (C) LSVs of different products measured on a RDE at 1200 rpm in 0.10 M PBS under light irradiation; (D) the photocatalytic H_2O_2 generation mechanism of α-Fe_2O_3/CQD@g-C_3N_4 featuring the Z-scheme charge transfer route.

In order to explore the behavior of water oxidation, the experiments for photocatalytic O_2 evolution with the developed composite were performed under visible light irradiation using $AgNO_3$ as the photoelectron quencher (Fig. S4†). Accordingly, an O_2 yield of 7.52 μmol in 4 h was obtained under visible light, corresponding to the rate of 62.7 μmol g^{-1} h^{-1} on average, indicating that the developed composite should conduct the photocatalytic water oxidation reaction so as to release the protons in water.

The rotating disk electrode (RDE) technique was first carried out to investigate the oxygen reduction abilities of different photocatalytic materials under light irradiation, and the results of linear sweep voltammetry (LSV) are shown in Fig. 8C. Accordingly, the α-Fe_2O_3/CQD@g-C_3N_4 could present the highest oxygen reduction ability, in contrast to α-Fe_2O_3 showing the lowest one. Particularly, the results show that the electrons in α-Fe_2O_3/CQD@g-C_3N_4 might be transferred from α-Fe_2O_3 to g-C_3N_4 under light irradiation. Moreover, DMPO–·O_2^- electron spin resonance (ESR) tests were comparably carried out for α-Fe_2O_3/CQD@g-C_3N_4 and CQD@g-C_3N_4 by the photo-degradation of methanol under visible light irradiation, and the results are shown in Fig. S5.† One can note that the developed α-Fe_2O_3/CQD@g-C_3N_4 can display four stronger characteristic peaks than the CQD@g-C_3N_4 under the same testing conditions, implying that the photo-generated electrons in the ternary composite might be transferred from α-Fe_2O_3 to g-C_3N_4. Furthermore, the water oxidation abilities of different photocatalysts were explored by the DMPO–·OH electron spin resonance tests under light irradiation (Fig. S6†). One can note that very weak characteristic peaks of DMPO–·OH could be observed for CQD@g-C_3N_4 after being illuminated for 10 min. However, an obvious enhancement of the DMPO–·OH ESR signal was obtained for α-Fe_2O_3/CQD@g-C_3N_4. It was found that the developed photocatalyst α-Fe_2O_3/CQD@g-C_3N_4 could present a much stronger water oxidation capability than CQD@g-C_3N_4. The ESR results are in good agreement with those of the RDE measurements, indicating that the as-fabricated α-Fe_2O_3/CQD@g-C_3N_4 might feature the Z-scheme charge transfer mechanism for the efficient photocatalytic reactions of H_2O_2 generation.

Based on the above investigations, a possible photocatalytic H_2O_2 generation pathway was proposed for the α-Fe_2O_3/CQD@g-C_3N_4 composite as schematically illustrated in Fig. 8D. One can find that the CQDs with the splendid up-conversion capacity could harvest light at a long wavelength up to 800 nm and emit at a short wavelength (<445 nm), which can correspond to the absorption edge of g-C_3N_4 as aforementioned. When exposing α-Fe_2O_3/CQD@g-C_3N_4 to the visible light range (420–800 nm), as shown in Fig. 8D, the excited electrons might be transferred from the CB of α-Fe_2O_3 to the VB of g-C_3N_4 due to the Z-scheme charge transfer pathway between g-C_3N_4 and α-Fe_2O_3. Furthermore, the excited electrons from the CB of g-C_3N_4 (−1.13 V *vs.* NHE) would be captured by CQDs, which might serve as electron acceptors so as to efficiently inhibit the recombination of charge carriers. Subsequently, the excited electrons on CQDs can directly restore O_2 into H_2O_2 (0.69 V *vs.* NHE). Not only that, owing to the EVB (2.43 V *vs.* NHE) of α-Fe_2O_3 being more positive than the $E(H_2O_2/H_2O)$ (1.76 V *vs.*

NHE), the photogenerated holes localized on α-Fe_2O_3 might oxidize H_2O into H_2O_2. What's more, when exposing α-Fe_2O_3/CQD@g-C_3N_4 to the near infrared light range ($\geq$800 nm), the photo-electrons might be transferred from the excited CQDs to the un-excited g-C_3N_4, and further to the un-excited α-Fe_2O_3. Ultimately, the oxygen might be restored by the electrons of α-Fe_2O_3 to yield H_2O_2 in the photocatalytic reaction with the developed composite.

Conclusions

In summary, ultrathin g-C_3N_4 nanosheets were successfully fabricated by a two-step precursor-regulated calcination route at a high heating rate of 30 °C min^{-1}, and they served as the carriers for the growth of carbon QDs and (110) exposed α-Fe_2O_3 to yield a ternary photocatalyst, namely the α-Fe_2O_3/CQD@g-C_3N_4 composite. Herein, the introduction of carbon QDs could extend its light absorption edge to the near infrared range (*i.e.*, 800 nm). Meanwhile, the loading of (110) exposed α-Fe_2O_3 could provide the active centers of the composite for the photocatalytic H_2O_2 generation. More importantly, it is evident that the (110) exposed α-Fe_2O_3 has converted the H_2O_2 generation route of α-Fe_2O_3/CQD@g-C_3N_4 from a two-step single-electron reduction into a direct one-step two-electron reduction. An improved charge carrier behavior could thus be expected for the significant enhancement of photocatalytic activities of the α-Fe_2O_3/CQD@g-C_3N_4 composite. Moreover, the developed green ternary photocatalyst could display highly efficient photocatalysis for H_2O_2 production at a rate of 1.16 μM min^{-1} under visible light irradiation, which is about 19 times faster than that of pure ultrathin g-C_3N_4. Also, the developed composite could exhibit an apparent quantum yield of 17.80% at 420 nm, which is even far more than that of commercially available TiO_2 (2.28%). This study opens a door towards the preparation of ultrathin g-C_3N_4 nanosheets simply by a green precursor-regulated calcination route. Also, it proposes an optimized photocatalytic pathway for the two-electron oxygen reduction for H_2O_2 production in pure water, without the use of any noble metal cocatalysts or organic scavengers. The further catalytic applications of the ternary photocatalyst in the medical and environmental fields such as disinfection and wastewater treatment will be investigated in future work.

Experimental section

Materials and instruments

Melamine ($C_3H_6N_6$, 99.0%), iron nitrate nonahydrate (98.5%), *N*,*N*-dimethylformamide (DMF, 99.5%), ethylene glycol (EG, 99.0%), isopropanol (IPA, 99.7%), nitroblue tetrazolium (NBT, 98.0%), and commercial titanium dioxide (TiO_2, 98.0%) were obtained from Sinopharm Chemical Reagent Co. Ltd. (Shanghai, China). Polyvinylpyrrolidone (PVP, MW $\approx$ 58 000, 99.5%) and *p*-benzoquinone (BQ, 97%) were purchased from Sigma-Aldrich Co. Ltd. (Shanghai, China). Horseradish peroxidase (HRP), *p*-hydroxyphenylacetic acid ($C_9H_{10}O_3$), potassium hydrogen phthalate ($C_8H_5KO_4$), and ethanol (C_2H_5OH) were used without further purification. Deionized water (>18.2 MΩ cm^{-1}) was used for all experiments (Pall, USA). A muffle furnace (Sx_2-10-12) with a high output (380 V/10 kW) was brought from Qixin Instruments Co. Ltd. (Shanghai, China).

Synthesis of photocatalytic materials

Synthesis of (110) exposed α-Fe_2O_3. α-Fe_2O_3 was fabricated through a modified solvothermal method previously reported.[31] Typically, an aliquot of 0.404 g of $Fe(NO_3)_3 \cdot 9H_2O$ and 0.60 g of PVP (MW 58 000) were dissolved in 36 mL of DMF. Then, the solution was transferred into a 70 mL Teflon-lined stainless steel autoclave, and heated at 180 °C for 12 h. After cooling, the precursor solution of α-Fe_2O_3 was preserved in the dark. Besides, the α-Fe_2O_3 precursor solution was centrifuged and washed separately with deionized water and ethanol several times. The obtained brown red products were dried at 60 °C to be stored for future use.

Synthesis of ultrathin g-C_3N_4. Ultrathin g-C_3N_4 nanosheets were fabricated by two-step calcination regulated by melamine precursors at a high heating rate in air. Typically, an aliquot of 0.50 g of melamine was dispersed in 15 mL of ethylene glycol. Then, 0.10 mM HNO_3 solution (30 mL) was slowly dropped into the mixture. The obtained white precipitate was centrifuged and washed with ethanol several times, followed by grinding to powder in an agate mortar after vacuum drying at 60 °C for 24 h. Subsequently, the powder was heated in a muffle furnace under ambient pressure at 450 °C for 2 h (30 °C min^{-1} heating rate) in air. After cooling to room temperature, the resulting light yellow powder was further annealed at 550 °C for another 2 h (30 °C min^{-1} heating rate) in air, forming the final yellow product of ultrathin g-C_3N_4 nanosheets.

Synthesis of CQD@g-C_3N_4. CQD@g-C_3N_4 composites were prepared through the growth of carbon QDs *in situ* onto g-C_3N_4 nanosheets. Typically, an aliquot of 0.10 g of g-C_3N_4 nanosheets was dispersed in a solution containing 13.6 mL of DMF and 16.4 mL of IPA under ultrasonic conditions. After stirring for 30 min, the mixture was transferred into a 70 mL autoclave to be heated at 180 °C for 8 h. The obtained yellow CQD@g-C_3N_4 composites were collected by centrifugation. After being washed with ethanol several times, the product was eventually dried at 60 °C for 12 h. (The preparation of carbon QDs can be seen in the ESI.†)

Synthesis of α-Fe_2O_3/CQD@g-C_3N_4. The preparation procedure of the α-Fe_2O_3/CQD@g-C_3N_4 nanocomposite is schematically illustrated in Scheme 1. Typically, an aliquot of 0.10 g of ultrathin g-C_3N_4 was dispersed in 16.4 mL of IPA. Afterwards, 13.6 mL of α-Fe_2O_3 precursor solution was introduced into the above mixed solution under vigorous stirring. After the ultrasonic dispersion for 30 min, the mixture was transferred into a 70 mL Teflon-lined autoclave to be heated at 180 °C for 8 h. Subsequently, the α-Fe_2O_3/CQD@g-C_3N_4 nanocomposites were collected by centrifugation and washed three times with ethanol, followed by drying at 60 °C overnight (the preparation of α-Fe_2O_3@g-C_3N_4 can be seen in the ESI†).

Photocatalytic tests

A photocatalytic testing apparatus composed of a glass reactor and an external illumination source was utilized in the

photocatalytic experiments according to the procedure previously reported.[56] A 300 W Xe-lamp (420 nm cut-off) was chosen as the visible light source (XL-300/Yirida Technology Co. Ltd.), with a distance of 20 cm from the reaction solution. Briefly, an aliquot of 5.0 mg of photocatalyst was first dispersed in 10 mL of water under sonication. All of the photocatalytic tests were carried out in pure water with the pH value at 7. The mixtures were stirred for 1 h in darkness so as to reach the adsorption–desorption equilibrium between the photocatalyst and oxygen in solution for the O_2-equilibrated tests. The O_2-saturated tests were implemented by bubbling O_2 for 15 min with further sustained O_2 flow until the experiments ended. During the illumination, 500 μL of reaction solution was taken from the reactor at a certain time interval, from which the photocatalyst powder was removed by centrifugation. Furthermore, 300 μL of the resulting supernatant liquid was measured using a fluorescence spectrophotometer (Fluoromax-4/Horiba) to acquire the changing fluorescence intensities according to the POHPAA analysis method.[57] The so obtained calibration curve for the fluorescence intensities *versus* H_2O_2 concentrations is presented in Fig. S7.† Besides, the $\cdot O_2^-$ scavenger experiments were further evaluated by the transformation of nitroblue tetrazolium (NBT) during photocatalytic H_2O_2 production.[48] The absorbance of NBT was determined using a UV-vis spectrophotometer (Shimadzu/UV-3600) at its characteristic absorbance peak around 260 nm.

The measurements of apparent quantum yields (AQYs) were simultaneously conducted during the H_2O_2 production of α-Fe_2O_3/CQD@g-C_3N_4 with various band-pass filters (420 nm, 450 nm, 600 nm, and 700 nm). The AQYs were calculated using the following equation:[52]

$$\mathrm{AQY} = \frac{N_e}{N_p} \times 100\% = \frac{N(H_2O_2) \times 2}{N(\mathrm{photons})} \times 100\% = \frac{2 \times M \times N_A \times h \times c}{S \times P \times t \times \lambda}$$

where N_e represents the reaction electrons, N_p represents the incident photons, M refers to the amount of H_2O_2 molecules, P is the light intensity determined using a photoradiometer (PL-MW 2000/PerfectLight), S is the light irradiation area, N_A represents the Avogadro constant, c is the speed of light, λ is the wavelength of the monochromatic light, h is the Planck constant, and t represents the photoreaction time.

Conflicts of interest

There are no conflicts to declare.

Acknowledgements

This work is supported by the National Natural Science Foundation of China (No. 21675099), the Major Basic Research Program of the Natural Science Foundation of Shandong Province (ZR2018ZC0129), and the Science and Technology Development Project of Weihai City (2015DXGJZD002), P. R. China.

References

1 J. M. Campos-Martin, G. Blanco-Brieva and J. L. Fierro, Hydrogen peroxide synthesis: An outlook beyond the anthraquinone process, *Angew. Chem., Int. Ed.*, 2006, **45**, 6962–6984.
2 I. H. Kim, *et al.*, Classification of the degradability of 30 pharmaceuticals in water with ozone, UV and H_2O_2, *Water Sci. Technol.*, 2008, **57**, 195–200.
3 B. Hu, *et al.*, Carbon-supported palladium catalysts for the direct synthesis of hydrogen peroxide from hydrogen and oxygen, *J. Catal.*, 2014, **319**, 15–26.
4 L. Wang, *et al.*, Mesoporous TiO_2 mixed crystals for photocatalytic pure water splitting, *Sci. China Mater.*, 2020, **63**, 758–768.
5 N. Lu, *et al.*, Characterization of highly effective plasma-treated g-C_3N_4 and application to the photocatalytic H_2O_2 production, *Chemosphere*, 2020, **241**, 124927.
6 L. Wang, S. Cao, K. Guo, Z. Wu, Z. Ma and L. Piao, Simultaneous hydrogen and peroxide production by photocatalytic water splitting, *Chin. J. Catal.*, 2019, **40**, 470–475.
7 X. Chen, Y. Kuwahara, K. Mori, C. Louisd and H. Yamashita, A hydrophobic titanium doped zirconium-based metal organic framework for photocatalytic hydrogen peroxide production in a two-phase system, *J. Mater. Chem. A*, 2020, **8**, 1904–1910.
8 Y. Zhang and S. J. Park, Formation of hollow MoO_3/SnS_2 heterostructured nanotubes for efficient light-driven hydrogen peroxide production, *J. Mater. Chem. A*, 2018, **6**, 20304–20312.
9 W. Hou and Y. Wang, Photocatalytic Generation of H_2O_2 by graphene oxide in organic electron donor-free condition under sunlight, *ACS Sustainable Chem. Eng.*, 2017, **5**, 2994–3001.
10 Y. Zeng, *et al.*, A three-dimensional graphitic carbon nitride belt network for enhanced visible light photocatalytic hydrogen evolution, *J. Mater. Chem. A*, 2016, **4**, 19003–19010.
11 Y. Gong, B. Yang, H. Zhang and X. Zhao, A g-C_3N_4/MIL-101(Fe) heterostructure composite for highly efficient BPA degradation with persulfate under visible light irradiation, *J. Mater. Chem. A*, 2018, **6**, 23703–23711.
12 M. Li, *et al.*, Core-shell $LaPO_4$/g-C_3N_4 nanowires for highly active and selective CO_2 reduction, *Appl. Catal., B*, 2017, **201**, 629–635.
13 H. Zhang, *et al.*, Functional carbon nitride materials for water oxidation: from heteroatom doping to interface engineering, *Nanoscale*, 2020, **12**, 6937–6952.
14 L. Zhou, *et al.*, Recent advances in non-metal modification of graphitic carbon nitride for photocatalysis: a historic review, *Catal. Sci. Technol.*, 2016, **6**, 7002–7023.
15 D. Ren, *et al.*, In situ fabrication of robust cocatalyst-free CdS/g-C3N4 2D-2D step-scheme heterojunctions for highly active H2 evolution, *Sol. RRL*, 2019, 1900423.
16 X. Li, J. Xiong, Y. Xu, Z. Feng and J. Huang, Defect-assisted surface modification enhances the visible light

photocatalytic performance of g-C_3N_4@C-TiO_2 direct Z-scheme heterojunctions, *Chin. J. Catal.*, 2019, **40**, 424–433.
17 L. Hu, J. Yan, C. Wang, B. Chai and J. Li, Direct electrospinning method for the construction of Z-scheme TiO_2/g-C3N_4/RGO ternary heterojunction photocatalysts with remarkably ameliorated photocatalytic performance, *Chin. J. Catal.*, 2019, **40**, 458–469.
18 Y. Ren, D. Zeng and W. J. Ong, Interfacial engineering of graphitic carbon nitride (g-C_3N_4)-based metal sulfide heterojunction photocatalysts for energy conversion: A review, *Chin. J. Catal.*, 2019, **40**, 289–319.
19 Y. Chen, *et al.*, Enhanced driving force and charge separation efficiency of protonated g-C_3N_4 for photocatalytic O_2 evolution, *ACS Catal.*, 2015, **5**, 6973–6979.
20 Y. Chen, *et al.*, Enhanced charge separation efficiency accelerates hydrogen evolution from water of carbon nitride and 3,4,9,10-perylene-tetracarboxylic dianhydride composite photocatalyst, *ACS Appl. Mater. Interfaces*, 2018, **10**(4), 3515–3521.
21 K. He, *et al.*, Enhanced visible light photocatalytic H_2 production over Z-scheme g-C_3N_4 nansheets/WO_3 nanorods nanocomposites loaded with $Ni(OH)_x$ cocatalysts, *Chin. J. Catal.*, 2017, **38**, 240–252.
22 W. Iqbal, *et al.*, One-step large-scale highly active g-C_3N_4 nanosheets for efficient sunlight-driven photocatalytic hydrogen production, *Dalton Trans.*, 2017, **46**, 10678–10684.
23 S. Kumar, T. Surendar, A. Baruahb and V. Shanker, Synthesis of a novel and stable g-C_3N_4-Ag_3PO_4 hybrid nanocomposite photocatalyst and study of the photocatalytic activity under visible light irradiation, *J. Mater. Chem. A*, 2013, **1**, 5333–5340.
24 Y. Chen, X. Liu, L. Hou, X. Guo, R. Fu and J. Sun, Construction of covalent bonding oxygen-doped carbon nitride/graphitic carbon nitride Z-scheme heterojunction for enhanced visible-light-driven H_2 evolution, *Chem. Eng. J.*, 2020, **383**, 123132.
25 Y. Xu, *et al.*, High-performance photoelectrochemical aptasensor for enrofloxacin based on Bi-doped ultrathin polymeric carbon nitride nanocomposites with SPR effect and carbon vacancies, *Sens. Actuators, B*, 2020, **316**, 128142.
26 L. Zhao, *et al.*, The synthesis of interface-modulated ultrathin Ni(ii) MOF/g-C_3N_4 heterojunctions as efficient photocatalysts for CO_2 reduction, *Nanoscale*, 2020, **12**, 10010–10018.
27 P. Yan, X. She and X. Zhu, Efficient photocatalytic hydrogen evolution by engineering amino groups into ultrathin 2D graphitic carbon nitride, *Appl. Surf. Sci.*, 2020, **507**, 145085.
28 W. Zhao, *et al.*, Single-atom Pt supported on holey ultrathin g-C_3N_4 nanosheets as efficient catalyst for Li-O_2 batteries, *J. Colloid Interface Sci.*, 2020, **564**, 28–36.
29 H. Che, *et al.*, Band structure engineering and efficient injection rich-π-electrons into ultrathin g-C_3N_4 for boosting photocatalytic H_2-production, *Appl. Surf. Sci.*, 2020, **505**, 144564.
30 J. H. Zhang, *et al.*, A facile method for scalable synthesis of ultrathin g-C_3N_4 nanosheets for efficient hydrogen production, *J. Mater. Chem. A*, 2018, **6**, 18252–18257.
31 B. Li, *et al.*, Anchoring single-unit-cell defect-rich bismuth molybdate layers on ultrathin carbon nitride nanosheet with boosted charge transfer for efficient photocatalytic ciprofloxacin degradation, *J. Colloid Interface Sci.*, 2020, **560**, 701–713.
32 X. Zhang, W. Wei, S. Zhang, B. Wen and Z. Su, Advanced 3D nanohybrid foam based on graphene oxide: Facile fabrication strategy, interfacial synergetic mechanism, and excellent photocatalytic performance, *Sci. China Mater.*, 2019, **62**, 1888–1897.
33 X. Wei, Y. Wang, Y. Huang and C. Fan, Composite ZIF-8 with CQDs for boosting visible-light-driven photocatalytic removal of NO, *J. Alloys Compd.*, 2019, **802**, 467–476.
34 Y. Zheng, *et al.*, Quasicubic α-Fe_2O_3 nanoparticles with excellent catalytic performance, *J. Phys. Chem. B*, 2006, **110**, 3093–3097.
35 W. Xing, *et al.*, Doping effect of non-metal group in porous ultrathin g-C_3N_4 nanosheets towards synergistically improved photocatalytic hydrogen evolution, *Nanoscale*, 2018, **10**, 5239–5245.
36 J. Hu, X. Zhao, W. Chen and Z. Chen, Enhanced charge transport and increased active sites on alpha-Fe_2O_3 (110) nanorod surface containing oxygen vacancies for improved solar water oxidation performance, *ACS Omega*, 2018, **3**, 14973–14980.
37 R. Shen, L. Zhang, X. Chen, M. Jaroniec, N. Li and X. Li, Integrating 2D/2D CdS/α-Fe_2O_3 ultrathin bilayer Z-scheme heterojunction with metallic β-NiS nanosheet-based ohmic-junction for efficient photocatalytic H_2 evolution, *Appl. Catal., B*, 2020, **266**, 118619.
38 H. Wu, T. Yang, Y. Du, L. Shen and G. W. Ho, Identification of facet-governing reactivity in hematite for oxygen evolution, *Adv. Mater.*, 2018, **30**, 1804341.
39 Y. Li, *et al.*, Ultrathin g-C_3N_4 nanosheets coupled with $AgIO_3$ as highly efficient heterostructured photocatalysts for enhanced visible-light photocatalytic activity, *Chem. – Eur. J.*, 2015, **21**, 17739–17747.
40 Z. Lu, *et al.*, Construction 0D/2D heterojunction by highly dispersed Ni_2P QDs loaded on the ultrathin g-C_3N_4 surface towards superhigh photocatalytic and photoelectric performance, *Appl. Catal., B*, 2018, **237**, 919–926.
41 Y. Deng, *et al.*, Construction of plasmonic Ag modified phosphorous-doped ultrathin g-C_3N_4 nanosheets/$BiVO_4$ photocatalyst with enhanced visible-near-infrared response ability for ciprofloxacin degradation, *J. Hazard. Mater.*, 2018, **344**, 758–769.
42 R. Huang, *et al.*, Enhanced photocatalytic fuel denitrification over TiO_2/alpha-Fe_2O_3 nanocomposites under visible light irradiation, *Sci. Rep.*, 2017, **7**, 7858.
43 X. Chen, *et al.*, Multi-pathway photoelectron migration in globular flower-like In_2O_3/AgBr/Bi_2WO_6 synthesized by microwave-assisted method with enhanced photocatalytic activity, *J. Mol. Catal. A: Chem.*, 2016, **414**, 27–36.
44 C. Chang, L. Zhu, S. Wang, X. Chu and L. Yue, Novel mesoporous graphite carbon nitride/BiOI heterojunction for enhancing photocatalytic performance under visible-

light irradiation, *ACS Appl. Mater. Interfaces*, 2014, **6**, 5083–5093.

45 T. Yan, *et al.*, Polymorph selection towards photocatalytic gaseous CO_2 hydrogenation, *Nat. Commun.*, 2019, **10**, 2521.

46 R. Lin, *et al.*, Quantitative study of charge carrier dynamics in well-defined WO_3 nanowires and nanosheets: Insight into the crystal facet effect in photocatalysis, *J. Am. Chem. Soc.*, 2018, **140**, 9078–9082.

47 Y. You, S. Wang, K. Xiao, T. Ma, Y. Zhang and H. Huang, Z-scheme g-C_3N_4/Bi_4NbO_8Cl heterojunction for enhanced photocatalytic hydrogen production, *ACS Sustainable Chem. Eng.*, 2018, **6**, 16219–16227.

48 Y. Yang, *et al.*, Ti_3C_2 Mxene/porous g-C_3N_4 interfacial Schottky junction for boosting spatial charge separation in photocatalytic H_2O_2 production, *Appl. Catal., B*, 2019, **258**, 117956.

49 T. Yan, *et al.*, Ultra-low loading of Ag_3PO_4 on hierarchical In_2S_3 microspheres to improve the photocatalytic performance: The cocatalytic effect of Ag and Ag_3PO_4, *Appl. Catal., B*, 2017, **202**, 84–94.

50 J. Zhang, *et al.*, Hollow sphere TiO_2-ZrO_2 prepared by self-assembly with polystyrene colloidal template for both photocatalytic degradation and H_2 evolution from water splitting, *ACS Sustainable Chem. Eng.*, 2016, **4**, 2037–2046.

51 Z. Jiang, W. Wan, H. Li, S. Yuan, H. Zhao and P. K. Wong, A hierarchical Z-scheme alpha-Fe_2O_3/g-C_3N_4 hybrid for enhanced photocatalytic CO_2 reduction, *Adv. Mater.*, 2018, **30**, 201706108.

52 R. Ma, *et al.*, Solid acids accelerate the photocatalytic hydrogen peroxide synthesis over a hybrid catalyst of titania nanotube with carbon dot, *Appl. Catal., B*, 2019, **244**, 594–603.

53 C. Liang, *et al.*, Construction of 2D heterojunction system with enhanced photocatalytic performance: Plasmonic Bi and reduced graphene oxide co-modified Bi_5O_7I with high-speed charge transfer channels, *J. Hazard. Mater.*, 2019, **361**, 245–258.

54 Y. He, L. Zhang, B. Teng and M. Fan, New application of Z-scheme Ag_3PO_4/g-C_3N_4 composite in converting CO_2 to fuel, *Environ. Sci. Technol.*, 2014, **49**, 649–656.

55 Q. Lv, *et al.*, Pyridinic nitrogen exclusively doped carbon materials as efficient oxygen reduction electrocatalysts for Zn-air batteries, *Appl. Catal., B*, 2020, **261**, 118234.

56 X. Chen, *et al.*, Effective photocatalytic salicylic acid removal under visible light irradiation using Ag_2S/AgI-Bi_2S_3/BiOI with Z-scheme heterojunctions, *Appl. Surf. Sci.*, 2019, **481**, 1335–1343.

57 A. L. Lazrus, G. L. Kok, S. N. Gitlin, J. A. Lind and S. E. McLaren, Automated fluorimetric method for hydrogen peroxide in atmospheric precipitation, *Anal. Chem.*, 1985, **57**, 917–922.